

## Article

# Luminescence Properties of Ho<sub>2</sub>O<sub>3</sub>-Doped Y<sub>2</sub>O<sub>3</sub> Stabilized ZrO<sub>2</sub> Single Crystals

Yuhua Yang, Shoulei Xu, Siyao Li, Wenxia Wu, Yihua Pan, Daini Wang, Xing Hong, Zeyu Cheng and Wen Deng \*

School of Physical Science and Technology, Guangxi University, 100 East Daxue Road, Nanning 530004, China; 1907301101@st.gxu.edu.cn (Y.Y.); xsl@gxu.edu.cn (S.X.); 1807301030@st.gxu.edu.cn (S.L.); 1907301088@st.gxu.edu.cn (W.W.); 1907301064@st.gxu.edu.cn (Y.P.); 1807301058@st.gxu.edu.cn (D.W.); 1807301016@st.gxu.edu.cn (X.H.); 2007301021@st.gxu.edu.cn (Z.C.)

\* Correspondence: wdeng@gxu.edu.cn; Tel.: +86-771-323-2666

**Abstract:** Single crystals of Ho<sub>2</sub>O<sub>3</sub>-doped Y<sub>2</sub>O<sub>3</sub> stabilized ZrO<sub>2</sub> (YSZ) with different Y<sub>2</sub>O<sub>3</sub> and Ho<sub>2</sub>O<sub>3</sub> contents were grown by the optical floating zone method. XRD and Raman spectra were measured and showed that crystal samples all had tetragonal structures. Measurements of positron annihilation lifetime spectra indicated that the increase in Y<sub>2</sub>O<sub>3</sub> concentration led to the increases of defects and mean positron lifetime, which enhanced the scattering of light and reduced the luminous intensity and the quantum yield (QY) of the crystal. Under the excitation at 446 nm, photoluminescence (PL) spectra of Ho<sub>2</sub>O<sub>3</sub>-doped YSZ crystals showed emission peaks at 540, 551, 670, and 757 nm corresponding to Ho<sup>3+</sup> transitions from <sup>5</sup>S<sub>2</sub>, <sup>5</sup>F<sub>4</sub>, <sup>5</sup>F<sub>5</sub>, and <sup>5</sup>I<sub>4</sub> excited states to the <sup>5</sup>I<sub>8</sub> ground state, respectively. At low Ho<sub>2</sub>O<sub>3</sub>-doped concentrations (0.10–0.50 mol%), the overall emission intensity increased with Ho<sub>2</sub>O<sub>3</sub> contents, reached the maximum value at 0.50 mol%, then decreased with higher Ho<sub>2</sub>O<sub>3</sub> contents, probably as a result of increased non-radiative relaxation caused by increased interactions between Ho<sup>3+</sup> ions. Quenching of the PL occurred at Ho<sub>2</sub>O<sub>3</sub> concentrations > 0.5 mol% and due to the electric dipole–dipole interaction. The calculated chromaticity coordinates (CIE) were approximately (0.307, 0.683) and the color purity achieved 99.6%. The results showed that Ho<sub>2</sub>O<sub>3</sub>: YSZ crystals were suitable for green light-emitting devices.

**Keywords:** yttria-stabilized zirconia; Ho<sub>2</sub>O<sub>3</sub> doped; luminescence properties; defects; optical floating zone method



**Citation:** Yang, Y.; Xu, S.; Li, S.; Wu, W.; Pan, Y.; Wang, D.; Hong, X.; Cheng, Z.; Deng, W. Luminescence Properties of Ho<sub>2</sub>O<sub>3</sub>-Doped Y<sub>2</sub>O<sub>3</sub> Stabilized ZrO<sub>2</sub> Single Crystals. *Crystals* **2022**, *12*, 415. <https://doi.org/10.3390/cryst12030415>

Academic Editors: Pavel Lukáč and Alessandro Chiasera

Received: 28 January 2022

Accepted: 15 March 2022

Published: 17 March 2022

**Publisher's Note:** MDPI stays neutral with regard to jurisdictional claims in published maps and institutional affiliations.



**Copyright:** © 2022 by the authors. Licensee MDPI, Basel, Switzerland. This article is an open access article distributed under the terms and conditions of the Creative Commons Attribution (CC BY) license (<https://creativecommons.org/licenses/by/4.0/>).

## 1. Introduction

Rare-earth doped materials have many valuable properties and have potential applications in display [1], lasers [2], solar cells [3], optical amplifier [4], mid-infrared fiber amplifiers [5], optical communication [6], etc. Rare earth ion Ho<sup>3+</sup> has absorption bands in both ultra-violet and visible regions and generates highly intensified emission, especially in the green region [7]. Many studies [8–10] have shown that Ho could be used as an element in white light production for its green emission. To investigate the emission characteristics of Ho<sup>3+</sup>, they must be incorporated into the right host.

Host materials could be in the form of glasses, powders, ceramics, or crystals. Metal oxide crystals have the highest physical and chemical stability and emission efficiency and doped rare-earth (RE) oxide crystals with high optical quality for use in laser physics have been developed over the past half-century [11]. As a host matrix for photonics and industrial applications, zirconia was attracted for its favorable properties, such as high hardness and refractive index, wide optical band gap, low optical loss, and high transparency from near-infrared to visible light [12]. ZrO<sub>2</sub> has significant technological applications such as fuel cells [13], catalysis [14], gas sensors [15], and optoelectronic devices [16]. Ho<sub>2</sub>O<sub>3</sub>: YSZ crystal has a promising application for visible light emission devices.

ZrO<sub>2</sub> could exist in three crystal structures: monoclinic, tetragonal, and cubic. At ambient temperature, the monoclinic phase was the stable form, and it transforms into the

tetragonal phase at 1170–2370 °C and the cubic phase at temperatures above 2370 °C to its melting point at 2716 °C [17,18]. There was a transition from the tetragonal phase to the monoclinic phase during the preparation of zirconia from high temperature to room temperature. This transition caused a volume expansion of 4.5%, which caused the crystal to crack [18]. The addition of certain kinds of oxides such as  $Y_2O_3$ ,  $TiO_2$ ,  $CaO$ , and  $CeO_2$  to pure  $ZrO_2$  stabilized a cubic or tetragonal phase down to room temperatures [19,20].  $Y_2O_3$  was the most common oxide additive. Both Y(III) and Zr(IV) have closed-shell electronic configurations and no transitions that could interfere with those of  $Ho^{3+}$ . The tetragonal or cubic phase could be stabilized by adding  $Y_2O_3$  [21]. High-quality crystals could be grown using the optical floating zone method [22].

Zirconia single crystals stabilized with 6 mol%, 8 mol%, and 10 mol%  $Y_2O_3$ , referred to as 6YSZ, 8YSZ, and 10YSZ, respectively, have been grown by the optical floating zone method by our group. It has been found that the growth quality and light transmittance of 8YSZ and 10YSZ crystals were good, while the 6YSZ crystal was not a transparency material. As  $RE^{3+}$  replaced  $Zr^{4+}$  in YSZ crystals, defects such as oxygen vacancies were created to maintain charge balance and zirconia was stabilized in the tetragonal or cubic phase. The luminescence efficiency depended on the luminescent rare-earth ions and substrates. In addition to luminescent ion concentration, the concentration of the stabilizer also affected the luminescence of the crystal. In the  $ZrO_2$  crystal, doping different concentrations of stabilizer  $Y_2O_3$  would produce defects due to charge compensation, and the defects influenced the luminescence of the crystal. It is very important to study the influence of defects and rare ions on the luminescence properties of the crystals.

In this paper, a series of  $(ZrO_2)_{90}(Y_2O_3)_{10-x}(Ho_2O_3)_x$  ( $x = 0.00, 0.10, 0.20, 0.30, 0.50, 0.75, 1.00, 1.20$ ),  $(ZrO_2)_{92}(Y_2O_3)_8$ , and  $(ZrO_2)_{92}(Y_2O_3)_{7.25}(Ho_2O_3)_{0.75}$  single crystals were grown by optical floating zone method. The microstructures and optical properties of the crystals were investigated by a variety of physical techniques, including X-ray diffraction (XRD), Raman spectroscopy, positron annihilation lifetime spectroscopy (PALS), UV-Visible Spectrophotometry (UV-Vis), photoluminescence (PL), and photoluminescence excitation (PLE).

## 2. Materials and Methods

### 2.1. Ceramic Rods Preparation

High purity oxide powders of  $Ho_2O_3$  (99.99%),  $Y_2O_3$  (99.99%), and  $ZrO_2$  (99.99%) were mixed in molar percentage composition of  $(ZrO_2)_{90}(Y_2O_3)_{10-x}(Ho_2O_3)_x$  ( $x = 0.00, 0.10, 0.20, 0.30, 0.50, 0.75, 1.00, 1.20$ ). For comparison,  $(ZrO_2)_{92}(Y_2O_3)_8$  and  $(ZrO_2)_{92}(Y_2O_3)_{7.25}(Ho_2O_3)_{0.75}$  samples were also prepared. The chemical compositions of  $Ho_2O_3$ -doped YSZ samples were shown in Table 1. Powders were put in ethanol and stirred with a magnetic stirrer for 24 h to ensure the various components in homogenization. Dry powder was obtained by drying suspension for 24 h and pouring into an agate mortar to ground thoroughly. The dried powder was formed into cylinders in a mold and then sintered at 1500 °C in a muffle furnace to produce ceramic rods.

### 2.2. Crystal Growth

For crystal production, the sintered ceramic rods were used as a raw material in an optical floating zone furnace (model: FZ-T-12000-X-VII-VPO-GU-PC, Crystal Systems Co., Kobchisawa, Japan).

Two ceramic rods with the same chemical composition but different lengths were used as feed and seed rods during crystal growth. The furnace consists of four 3-kilowatt Xe lamps that were focused by four polished elliptical mirrors to form a molten zone between the feed and the seed rods. The power was adjusted to produce a stable melting zone. In the process of crystal growth, the feed and seed rods were rotated in opposite directions to improve uniformity, and then they were moved down at a speed of 5 mm/h for crystallization. The crystals rods grown by this method are shown in Figure 1. They were transparent, large, and uniform, with no obvious cracks or impurity phases. Discs of

1 mm thickness were cut using a crystal cutter from the crystals. The surfaces of the discs were polished with a single shaft polisher for investigations of optical properties. The XRD powder samples were ground from the crystals.

**Table 1.** Chemical compositions of Ho<sub>2</sub>O<sub>3</sub>-doped YSZ samples.

Samples	Composition mol%		
	ZrO <sub>2</sub>	Y <sub>2</sub> O <sub>3</sub>	Ho <sub>2</sub> O <sub>3</sub>
(ZrO <sub>2</sub> ) <sub>90</sub> (Y <sub>2</sub> O <sub>3</sub> ) <sub>10</sub>	90.00	10.00	0.00
(ZrO <sub>2</sub> ) <sub>90</sub> (Y <sub>2</sub> O <sub>3</sub> ) <sub>9.90</sub> (Ho <sub>2</sub> O <sub>3</sub> ) <sub>0.10</sub>	90.00	9.90	0.10
(ZrO <sub>2</sub> ) <sub>90</sub> (Y <sub>2</sub> O <sub>3</sub> ) <sub>9.80</sub> (Ho <sub>2</sub> O <sub>3</sub> ) <sub>0.20</sub>	90.00	9.80	0.20
(ZrO <sub>2</sub> ) <sub>90</sub> (Y <sub>2</sub> O <sub>3</sub> ) <sub>9.70</sub> (Ho <sub>2</sub> O <sub>3</sub> ) <sub>0.30</sub>	90.00	9.70	0.30
(ZrO <sub>2</sub> ) <sub>90</sub> (Y <sub>2</sub> O <sub>3</sub> ) <sub>9.50</sub> (Ho <sub>2</sub> O <sub>3</sub> ) <sub>0.50</sub>	90.00	9.50	0.50
(ZrO <sub>2</sub> ) <sub>90</sub> (Y <sub>2</sub> O <sub>3</sub> ) <sub>9.25</sub> (Ho <sub>2</sub> O <sub>3</sub> ) <sub>0.75</sub>	90.00	9.25	0.75
(ZrO <sub>2</sub> ) <sub>90</sub> (Y <sub>2</sub> O <sub>3</sub> ) <sub>9.00</sub> (Ho <sub>2</sub> O <sub>3</sub> ) <sub>1.00</sub>	90.00	9.00	1.00
(ZrO <sub>2</sub> ) <sub>90</sub> (Y <sub>2</sub> O <sub>3</sub> ) <sub>8.80</sub> (Ho <sub>2</sub> O <sub>3</sub> ) <sub>1.20</sub>	90.00	8.80	1.20
(ZrO <sub>2</sub> ) <sub>92</sub> (Y <sub>2</sub> O <sub>3</sub> ) <sub>8</sub>	92.00	8.00	0.00
(ZrO <sub>2</sub> ) <sub>92</sub> (Y <sub>2</sub> O <sub>3</sub> ) <sub>7.25</sub> (Ho <sub>2</sub> O <sub>3</sub> ) <sub>0.75</sub>	92.00	7.25	0.75

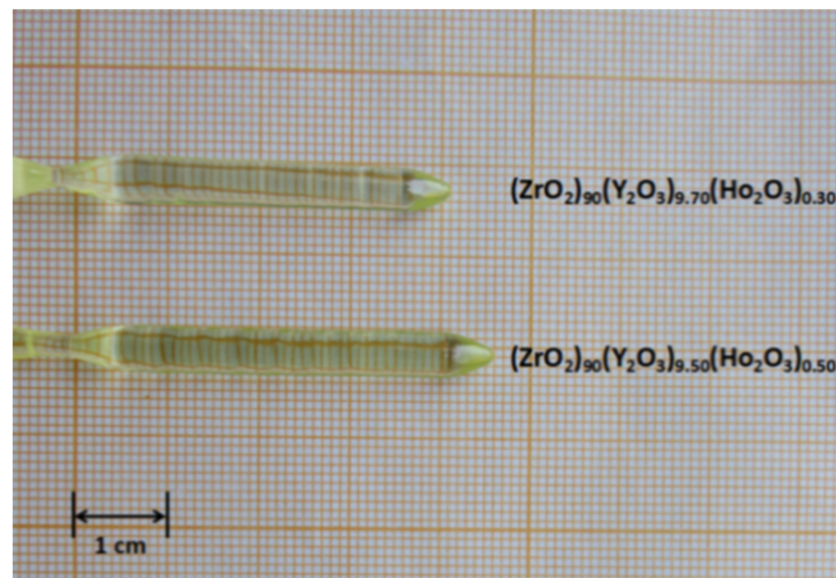


**Figure 1.** (ZrO<sub>2</sub>)<sub>90</sub>(Y<sub>2</sub>O<sub>3</sub>)<sub>9.70</sub>(Ho<sub>2</sub>O<sub>3</sub>)<sub>0.30</sub> and (ZrO<sub>2</sub>)<sub>90</sub>(Y<sub>2</sub>O<sub>3</sub>)<sub>9.50</sub>(Ho<sub>2</sub>O<sub>3</sub>)<sub>0.50</sub> crystal rods.

Analytical measurements were made on a (ZrO<sub>2</sub>)<sub>90</sub>(Y<sub>2</sub>O<sub>3</sub>)<sub>9.25</sub>(Ho<sub>2</sub>O<sub>3</sub>)<sub>0.75</sub> crystal disc using energy-dispersive X-ray (EDX) spectroscopy on our SEM instrument. The SEM–EDS measurements showed that all Zr, Y, Ho, and O elements were evenly distributed, and thus the doping elements were well dispersed in the crystal, as shown in Figure 2.

### 2.3. Sample Measurements

XRD patterns of the powder samples at room temperature were obtained with an X-ray diffractometer (Rigaku, Japan) using Cu K $\alpha$  radiation ( $\lambda = 0.15406$  nm) as the light source, and with 0.6°/s scan rate, and 0.02° step size within the scan range 20°–80° 2 $\theta$  diffraction angles. Raman spectra in the range 100–800 cm<sup>−1</sup> were obtained with a laser Raman spectrometer (Finder One, Zhuoli Hanguang Company, Beijing, China). Absorption spectra were obtained using a Shimadzu UV-2700 spectrometer. Positron annihilation lifetime spectra were acquired using an ORTEC fast-fast coincidence system with a time resolution of 250 ps. A <sup>22</sup>Na positron source (with an activity of about 3.7 × 10<sup>5</sup> Bq) was sandwiched between 2 polished disks. 1.28 MeV and 511 keV  $\gamma$ -rays as signals of positron produced and their annihilation. 10<sup>6</sup> counts were accumulated to produce a time-dependent spectrum.

The POSITRONFIT extended software program was used to analyze the positron lifetime spectra. The PL and PLE spectra were obtained by a photoluminescence spectrometry (ZLF-325 type, Beijing Zhuoli Hanguang Optical Instrument) at room temperature, using a 150 W Xe lamp as the excitation source.

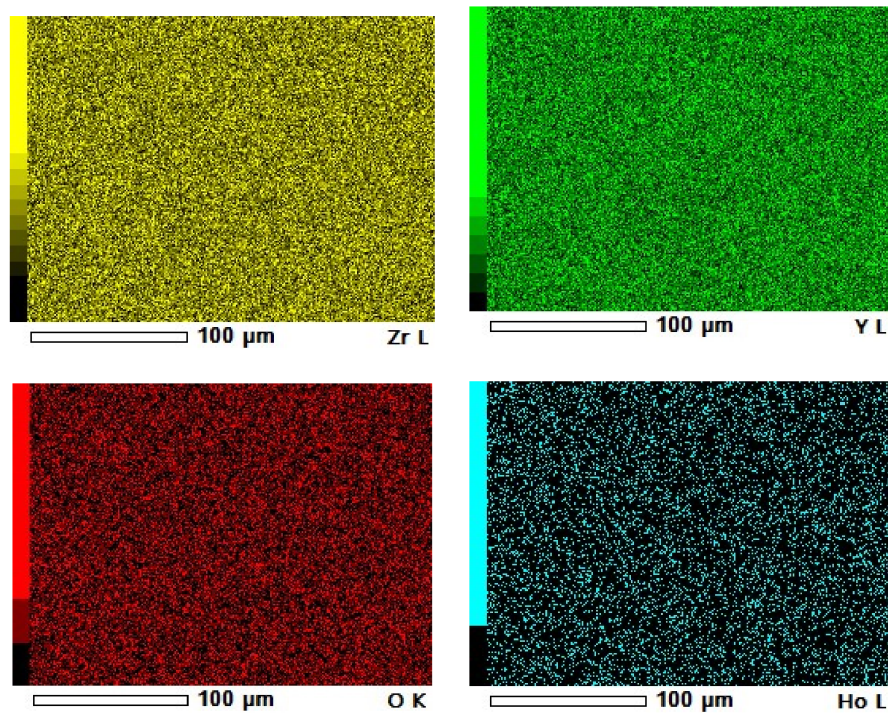


Figure 2. EDS image of the  $(\text{ZrO}_2)_{90}(\text{Y}_2\text{O}_3)_{9.25}(\text{Ho}_2\text{O}_3)_{0.75}$  sample.

### 3. Results and Discussion

#### 3.1. X-ray Diffraction (XRD)

The XRD patterns of the  $(\text{ZrO}_2)_{92}(\text{Y}_2\text{O}_3)_{7.25}(\text{Ho}_2\text{O}_3)_{0.75}$  and  $(\text{ZrO}_2)_{90}(\text{Y}_2\text{O}_3)_{9.25}(\text{Ho}_2\text{O}_3)_{0.75}$  powders ground from the crystals were shown in Figure 3, respectively. All samples had peaks at  $30.14^\circ$ ,  $35.02^\circ$ ,  $50.21^\circ$ ,  $59.70^\circ$ ,  $62.61^\circ$ , and  $73.66^\circ$  that corresponded to either the tetragonal or cubic phase. No additional peaks of a secondary phase were observed in the patterns, indicating that  $\text{Ho}^{3+}$  and  $\text{Y}^{3+}$  come into the  $\text{ZrO}_2$  lattice successfully.

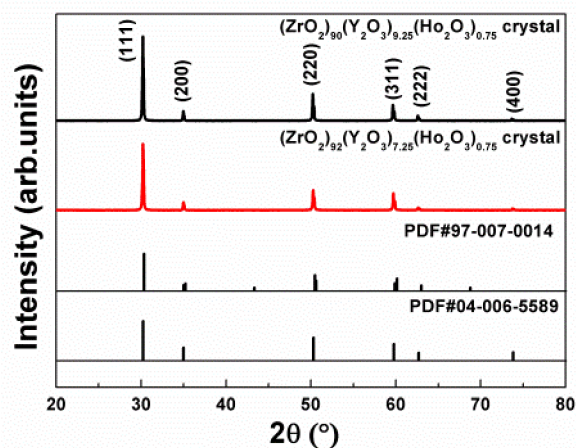
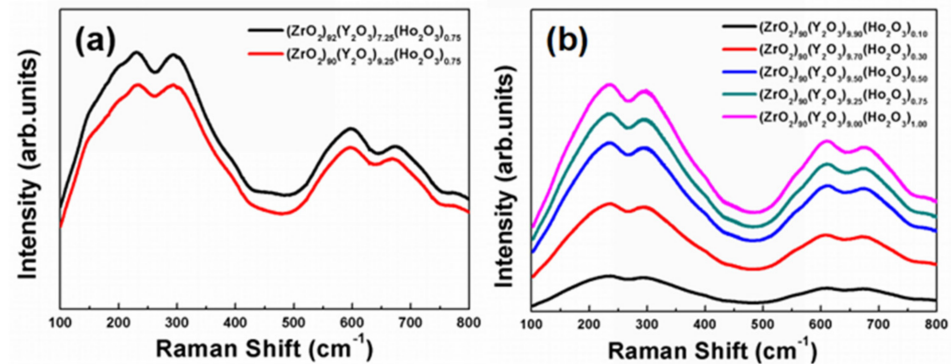


Figure 3. XRD patterns of  $(\text{ZrO}_2)_{92}(\text{Y}_2\text{O}_3)_{7.25}(\text{Ho}_2\text{O}_3)_{0.75}$  and  $(\text{ZrO}_2)_{90}(\text{Y}_2\text{O}_3)_{9.25}(\text{Ho}_2\text{O}_3)_{0.75}$  powders ground from the crystals.

### 3.2. Raman Spectroscopy

Because of the high degree of similarity in the XRD patterns from the tetragonal and cubic structures, additional measurements were needed to conclusively identify the phase composition of the  $\text{Ho}^{3+}$  doped YSZ samples. This could be achieved by Raman spectroscopy because the tetragonal phase produced six peaks ( $A_{1g} + 2B_{1g} + 3E_g$ ), while the cubic phase had only one active mode ( $F_{2g}$ ) [23]. The Raman spectra of all crystal samples were shown in Figure 4a,b; all contained peaks at about 237, 295, 406, 609, and  $680\text{ cm}^{-1}$ , and, thus, they were consistent with the tetragonal structure [24]. Therefore, the  $\text{Ho}^{3+}$  doped YSZ single crystal was a tetragonal structure.



**Figure 4.** (a) Raman spectra of  $(\text{ZrO}_2)_{92}(\text{Y}_2\text{O}_3)_{7.25}(\text{Ho}_2\text{O}_3)_{0.75}$  and  $(\text{ZrO}_2)_{90}(\text{Y}_2\text{O}_3)_{9.25}(\text{Ho}_2\text{O}_3)_{0.75}$ . (b) Raman spectra of  $(\text{ZrO}_2)_{90}(\text{Y}_2\text{O}_3)_{10-x}(\text{Ho}_2\text{O}_3)_x$ .

Combined with the XRD pattern, the results from the two crystals were very similar and indicative of a tetragonal structure. The crystal structure of the  $\text{Ho}_2\text{O}_3$  doped YSZ sample did not change with different concentrations of  $\text{Y}_2\text{O}_3$  and  $\text{Ho}_2\text{O}_3$ .

### 3.3. Positron Annihilation Lifetime Spectroscopy (PALS)

The type, size, and concentration of defects in the crystal could be analyzed according to positron lifetime parameters [25,26]. Positron annihilation lifetime spectra of  $(\text{ZrO}_2)_{92}(\text{Y}_2\text{O}_3)_{7.25}(\text{Ho}_2\text{O}_3)_{0.75}$  and  $(\text{ZrO}_2)_{90}(\text{Y}_2\text{O}_3)_{9.25}(\text{Ho}_2\text{O}_3)_{0.75}$  crystals were shown in Figure S1 (see Supplementary Materials). After source correction ( $\tau_s = 380\text{ ps}$ ,  $I_s = 8.0\%$ ) and background subtraction, the fitting results of PALS for  $\text{Ho}_2\text{O}_3$ -doped YSZ crystals were obtained with three decay components,  $\tau_1$ ,  $\tau_2$ , and  $\tau_3$  and relative intensities  $I_1'$ ,  $I_2'$  and  $I_3'$ . The third component  $\tau_3$  in each spectrum with intensity  $I_3'$  ( $<1\%$ ) resulted from the positron that was annihilated on the surface of the specimens. This was disregarded in our discussion. Let  $I_1 = I_1' / (I_1' + I_2')$ ,  $I_2 = I_2' / (I_1' + I_2')$  for renormalization of the intensities. The second component  $\tau_2$  was the lifetime of positron annihilated at microdefects. According to the standard trapping model [27,28], one could obtain the positron annihilation rate and the positron lifetime in the bulk ( $\lambda_b$  and  $\tau_b$ ):  $\lambda_b = I_1/\tau_1 + I_2/\tau_2$ ,  $\tau_b = 1/\lambda_b$ . The mean lifetime  $\tau_m$  was calculated by equation  $\tau_m = I_1\tau_1 + I_2\tau_2$  reflected the properties of all positron annihilation of the  $\text{Ho}_2\text{O}_3$ :YSZ sample. The positron lifetime parameters of the  $(\text{ZrO}_2)_{92}(\text{Y}_2\text{O}_3)_{7.25}(\text{Ho}_2\text{O}_3)_{0.75}$  and  $(\text{ZrO}_2)_{90}(\text{Y}_2\text{O}_3)_{9.25}(\text{Ho}_2\text{O}_3)_{0.75}$  crystals were listed in Table 2.

**Table 2.** Positron lifetime parameters of the  $(\text{ZrO}_2)_{92}(\text{Y}_2\text{O}_3)_{7.25}(\text{Ho}_2\text{O}_3)_{0.75}$  and  $(\text{ZrO}_2)_{90}(\text{Y}_2\text{O}_3)_{9.25}(\text{Ho}_2\text{O}_3)_{0.75}$  crystals.

Sample	$\tau_1$ (ps)	$\tau_2$ (ps)	$I_1$ (%)	$I_2$ (%)	$\lambda_b$ ( $\text{ns}^{-1}$ )	$\tau_b$ (ps)	$\tau_m$ (ps)
$(\text{ZrO}_2)_{92}(\text{Y}_2\text{O}_3)_{7.25}(\text{Ho}_2\text{O}_3)_{0.75}$	$193 \pm 1$	$482 \pm 26$	89.2	10.8	4.84	206	224
$(\text{ZrO}_2)_{90}(\text{Y}_2\text{O}_3)_{9.25}(\text{Ho}_2\text{O}_3)_{0.75}$	$191 \pm 1$	$436 \pm 14$	82.2	17.8	4.71	212	234

Except interstitial defects, open volume defects normally included vacancies, dislocations, grain boundaries, and bubbles. In comparison to the interstitial defects, open volume defects were more sensitive to positron annihilation techniques [29,30]. The bulk positron lifetime  $\tau_b > 200$  ps represented the low electron densities in the bulk of the crystals. It was obvious that the mean lifetime  $\tau_m$  and the  $I_2$  of the  $(\text{ZrO}_2)_{90}(\text{Y}_2\text{O}_3)_{9.25}(\text{Ho}_2\text{O}_3)_{0.75}$  crystal were larger than those of the  $(\text{ZrO}_2)_{92}(\text{Y}_2\text{O}_3)_{7.25}(\text{Ho}_2\text{O}_3)_{0.75}$  crystal. This meant that the concentration of open volume defects of the  $(\text{ZrO}_2)_{90}(\text{Y}_2\text{O}_3)_{9.25}(\text{Ho}_2\text{O}_3)_{0.75}$  crystal was higher than that of the  $(\text{ZrO}_2)_{92}(\text{Y}_2\text{O}_3)_{7.25}(\text{Ho}_2\text{O}_3)_{0.75}$  crystal. When some of the  $\text{Zr}^{4+}$  ions in the crystal lattice were replaced by trivalent rare-earth ions ( $\text{Y}^{3+}$  or  $\text{Ho}^{3+}$ ), defects such as oxygen vacancies were created to maintain charge balance. Obviously,  $(\text{ZrO}_2)_{90}(\text{Y}_2\text{O}_3)_{9.25}(\text{Ho}_2\text{O}_3)_{0.75}$  crystal had a higher  $\text{Y}_2\text{O}_3$  concentration, thus, it contained more defects.

### 3.4. The Luminescence Spectra of the $(\text{ZrO}_2)_{92}(\text{Y}_2\text{O}_3)_{7.25}(\text{Ho}_2\text{O}_3)_{0.75}$ and $(\text{ZrO}_2)_{90}(\text{Y}_2\text{O}_3)_{9.25}(\text{Ho}_2\text{O}_3)_{0.75}$ Crystals

Room temperature PLE spectrum of  $(\text{ZrO}_2)_{90}(\text{Y}_2\text{O}_3)_{9.25}(\text{Ho}_2\text{O}_3)_{0.75}$  crystal in the 300–500 nm range monitored at 551 nm was shown in Figure 5. It had seven peaks located at 356, 381, 415, 446, 452, 461, and 481 nm corresponding to the transitions from  $\text{Ho}^{3+} {}^5\text{I}_8$  ground state to the  ${}^5\text{G}_2$ ,  ${}^5\text{G}_4 + {}^3\text{K}_7$ ,  ${}^5\text{G}_5 + {}^3\text{G}_5$ ,  ${}^5\text{G}_6$ ,  ${}^5\text{F}_1$ ,  ${}^5\text{F}_2$ , and  ${}^5\text{F}_3$  energy levels states, respectively [31]. The sample produced spectrum with the band at 446 nm having the highest intensity. This wavelength was then used to excite the sample to produce the down-conversion PL spectrum.

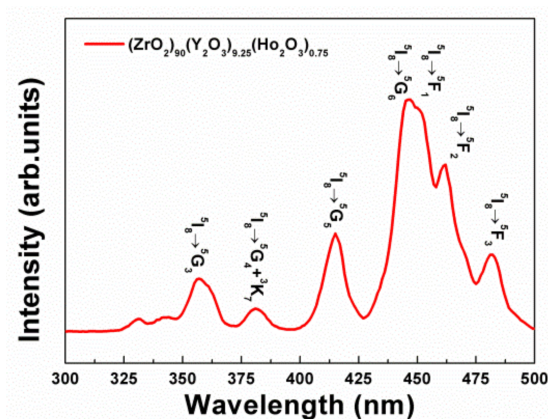
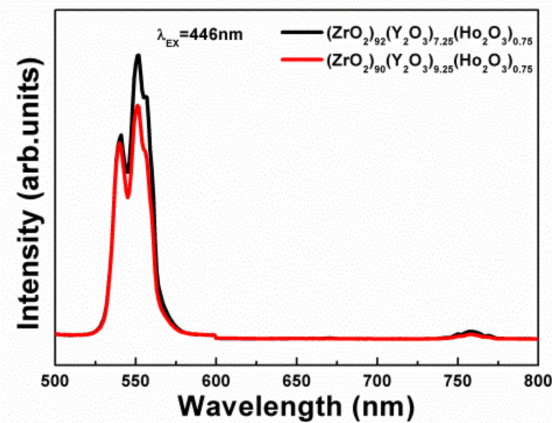


Figure 5. PLE spectrum monitored at 551 nm for  $(\text{ZrO}_2)_{90}(\text{Y}_2\text{O}_3)_{9.25}(\text{Ho}_2\text{O}_3)_{0.75}$  crystals.

The PL spectra for  $(\text{ZrO}_2)_{92}(\text{Y}_2\text{O}_3)_{7.25}(\text{Ho}_2\text{O}_3)_{0.75}$  and  $(\text{ZrO}_2)_{90}(\text{Y}_2\text{O}_3)_{9.25}(\text{Ho}_2\text{O}_3)_{0.75}$  crystals under the excitation at 446 nm were shown in Figure 6. Their spectral shape did not change with  $\text{Y}_2\text{O}_3$  concentration. As we know, the symmetry of the main material was an important factor affecting the luminescence intensity [32,33]. XRD and Raman spectra indicated that both crystal samples were tetragonal structures. In addition, the concentration of defects also affected the luminescence intensity of  $\text{RE}^{3+}$  [34].

The luminescence intensity of  $(\text{ZrO}_2)_{90}(\text{Y}_2\text{O}_3)_{9.25}(\text{Ho}_2\text{O}_3)_{0.75}$  crystal was weaker than that of  $(\text{ZrO}_2)_{92}(\text{Y}_2\text{O}_3)_{7.25}(\text{Ho}_2\text{O}_3)_{0.75}$  crystal, which was due to the higher concentration of  $\text{Y}_2\text{O}_3$ . As a result, the luminescence intensity of  $(\text{ZrO}_2)_{90}(\text{Y}_2\text{O}_3)_{9.25}(\text{Ho}_2\text{O}_3)_{0.75}$  crystal was lower than that of the  $(\text{ZrO}_2)_{92}(\text{Y}_2\text{O}_3)_{7.25}(\text{Ho}_2\text{O}_3)_{0.75}$  crystal.



**Figure 6.** PL spectra for  $(\text{ZrO}_2)_{92}(\text{Y}_2\text{O}_3)_{7.25}(\text{Ho}_2\text{O}_3)_{0.75}$  and  $(\text{ZrO}_2)_{90}(\text{Y}_2\text{O}_3)_{9.25}(\text{Ho}_2\text{O}_3)_{0.75}$  crystals under the excitation at 446 nm.

### 3.5. The Quantum Yields of the $(\text{ZrO}_2)_{92}(\text{Y}_2\text{O}_3)_{7.25}(\text{Ho}_2\text{O}_3)_{0.75}$ and $(\text{ZrO}_2)_{90}(\text{Y}_2\text{O}_3)_{9.25}(\text{Ho}_2\text{O}_3)_{0.75}$ Crystals

Figure 5 demonstrated that there was an absorption peak at 446 nm in the PLE spectrum of the  $(\text{ZrO}_2)_{90}(\text{Y}_2\text{O}_3)_{9.25}(\text{Ho}_2\text{O}_3)_{0.75}$  crystal. And a green light emission peak at 551 nm was found in the PL spectra of  $(\text{ZrO}_2)_{92}(\text{Y}_2\text{O}_3)_{7.25}(\text{Ho}_2\text{O}_3)_{0.75}$  and  $(\text{ZrO}_2)_{90}(\text{Y}_2\text{O}_3)_{9.25}(\text{Ho}_2\text{O}_3)_{0.75}$  crystals under the excitation at 446 nm as shown in Figure 6.

To measure the quantum yields of the  $(\text{ZrO}_2)_{92}(\text{Y}_2\text{O}_3)_{7.25}(\text{Ho}_2\text{O}_3)_{0.75}$  and  $(\text{ZrO}_2)_{90}(\text{Y}_2\text{O}_3)_{9.25}(\text{Ho}_2\text{O}_3)_{0.75}$  crystals, luminescence spectra in the 425–600 nm range of the  $(\text{ZrO}_2)_{90}(\text{Y}_2\text{O}_3)_{10}$ ,  $(\text{ZrO}_2)_{92}(\text{Y}_2\text{O}_3)_8$ ,  $(\text{ZrO}_2)_{92}(\text{Y}_2\text{O}_3)_{7.25}(\text{Ho}_2\text{O}_3)_{0.75}$ , and  $(\text{ZrO}_2)_{90}(\text{Y}_2\text{O}_3)_{9.25}(\text{Ho}_2\text{O}_3)_{0.75}$  crystals under the excitation at 446 nm were collected, as shown in Figure 7. The  $(\text{ZrO}_2)_{92}(\text{Y}_2\text{O}_3)_8$  and  $(\text{ZrO}_2)_{90}(\text{Y}_2\text{O}_3)_{10}$  crystals were the reference samples of the  $(\text{ZrO}_2)_{92}(\text{Y}_2\text{O}_3)_{7.25}(\text{Ho}_2\text{O}_3)_{0.75}$  and  $(\text{ZrO}_2)_{90}(\text{Y}_2\text{O}_3)_{9.25}(\text{Ho}_2\text{O}_3)_{0.75}$  crystals, respectively.

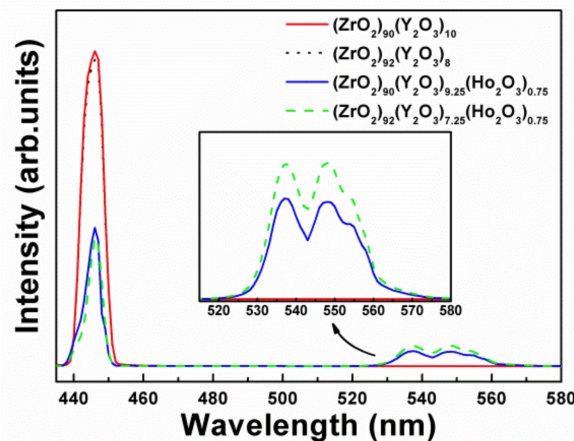


**Figure 7.** Luminescence spectra for  $(\text{ZrO}_2)_{90}(\text{Y}_2\text{O}_3)_{10}$ ,  $(\text{ZrO}_2)_{92}(\text{Y}_2\text{O}_3)_8$ ,  $(\text{ZrO}_2)_{92}(\text{Y}_2\text{O}_3)_{7.25}(\text{Ho}_2\text{O}_3)_{0.75}$ , and  $(\text{ZrO}_2)_{90}(\text{Y}_2\text{O}_3)_{9.25}(\text{Ho}_2\text{O}_3)_{0.75}$  crystals under the excitation at 446 nm.

Figure 7 indicated that there was an absorption band from 434 to 460 nm and a green light emission band from 521 to 575 nm in the luminescence spectra of  $(\text{ZrO}_2)_{92}(\text{Y}_2\text{O}_3)_{7.25}(\text{Ho}_2\text{O}_3)_{0.75}$  and  $(\text{ZrO}_2)_{90}(\text{Y}_2\text{O}_3)_{9.25}(\text{Ho}_2\text{O}_3)_{0.75}$  crystals.

QY (quantum yield) could be calculated by Equation (1) [35,36]:

$$\text{QY} = \frac{N_{em}}{N_{abs}} \quad (1)$$

where  $N_{abs}$  was the number of photons absorbed by a sample and  $N_{em}$  was the number of photons emitted from a sample. The quantum yields of the  $(ZrO_2)_{92}(Y_2O_3)_{7.25}(Ho_2O_3)_{0.75}$  and  $(ZrO_2)_{90}(Y_2O_3)_{9.25}(Ho_2O_3)_{0.75}$  crystals could be obtained by Formula (2) and (3), respectively.

$$QY_{(ZrO_2)_{92}(Y_2O_3)_{7.25}(Ho_2O_3)_{0.75}} = \frac{N_{em}}{N_{abs}} = \frac{\int_{521}^{575} N_{em}^{sam}(\lambda)d(\lambda) - \int_{521}^{575} N_{em}^{ref}(\lambda)d(\lambda)}{\int_{434}^{460} N_{ex}^{ref}(\lambda)d(\lambda) - \int_{434}^{460} N_{ex}^{sam}(\lambda)d(\lambda)} \quad (2)$$

$$QY_{(ZrO_2)_{90}(Y_2O_3)_{9.25}(Ho_2O_3)_{0.75}} = \frac{N_{em}}{N_{abs}} = \frac{\int_{521}^{575} N_{em}^{sam'}(\lambda)d(\lambda) - \int_{521}^{575} N_{em}^{ref'}(\lambda)d(\lambda)}{\int_{434}^{460} N_{ex}^{ref'}(\lambda)d(\lambda) - \int_{434}^{460} N_{ex}^{sam'}(\lambda)d(\lambda)} \quad (3)$$

where  $N_{em}^{sam}$  and  $N_{em}^{sam'}$  were the integrated intensities of the emission light of the  $(ZrO_2)_{92}(Y_2O_3)_{7.25}(Ho_2O_3)_{0.75}$  and  $(ZrO_2)_{90}(Y_2O_3)_{9.25}(Ho_2O_3)_{0.75}$  crystals.  $N_{em}^{ref}$  and  $N_{em}^{ref'}$  represented the integrated intensities of the emission light of the  $(ZrO_2)_{92}(Y_2O_3)_8$  and  $(ZrO_2)_{90}(Y_2O_3)_{10}$  crystals.  $N_{ex}^{ref}$  and  $N_{ex}^{ref'}$  were the integrated intensities of the excitation light of the  $(ZrO_2)_{92}(Y_2O_3)_8$  and  $(ZrO_2)_{90}(Y_2O_3)_{10}$  crystal.  $N_{ex}^{sam}$  and  $N_{ex}^{sam'}$  represented the integrated intensities of the excitation light of the  $(ZrO_2)_{92}(Y_2O_3)_{7.25}(Ho_2O_3)_{0.75}$  and  $(ZrO_2)_{90}(Y_2O_3)_{9.25}(Ho_2O_3)_{0.75}$  crystals, respectively. The quantum yields of the  $(ZrO_2)_{92}(Y_2O_3)_{7.25}(Ho_2O_3)_{0.75}$  and  $(ZrO_2)_{90}(Y_2O_3)_{9.25}(Ho_2O_3)_{0.75}$  crystals were listed in Table 3.

**Table 3.** The quantum yields of the  $(ZrO_2)_{92}(Y_2O_3)_{7.25}(Ho_2O_3)_{0.75}$  and  $(ZrO_2)_{90}(Y_2O_3)_{9.25}(Ho_2O_3)_{0.75}$  crystals.

Sample	$N_{abs}$ (Counts)	$N_{em}$ (Counts)	QY (%)
$(ZrO_2)_{92}(Y_2O_3)_{7.25}(Ho_2O_3)_{0.75}$	49,204,500	15,458,581	31.4
$(ZrO_2)_{90}(Y_2O_3)_{9.25}(Ho_2O_3)_{0.75}$	48,688,100	11,318,743	23.2

It was known that the defects in the crystals reduced the quantum yields [36,37]. The quantum yield of the  $(ZrO_2)_{90}(Y_2O_3)_{9.25}(Ho_2O_3)_{0.75}$  crystal was less than that of the  $(ZrO_2)_{92}(Y_2O_3)_{7.25}(Ho_2O_3)_{0.75}$  crystal, which was due to the higher concentration of  $Y_2O_3$ , more defects were generated, thus enhanced the scattering of light and decreased the probability of the light emission. As a result, the quantum yield of  $(ZrO_2)_{90}(Y_2O_3)_{9.25}(Ho_2O_3)_{0.75}$  crystal was lower than that of the  $(ZrO_2)_{92}(Y_2O_3)_{7.25}(Ho_2O_3)_{0.75}$  crystal. The results were consistent with that from Figure 6.

### 3.6. The Luminescence Properties of $(ZrO_2)_{90}(Y_2O_3)_{10-x}(Ho_2O_3)_x$

#### 3.6.1. Absorption Spectrum

The absorption spectrum of  $(ZrO_2)_{90}(Y_2O_3)_{9.25}(Ho_2O_3)_{0.75}$  crystal was shown in Figure 8.

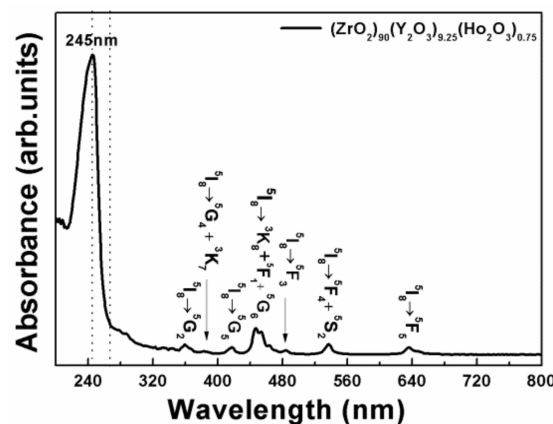


**Figure 8.** UV-vis absorption spectrum of the  $(ZrO_2)_{90}(Y_2O_3)_{9.25}(Ho_2O_3)_{0.75}$  crystal.

The absorption spectrum of the  $(\text{ZrO}_2)_{90}(\text{Y}_2\text{O}_3)_{9.25}(\text{Ho}_2\text{O}_3)_{0.75}$  crystal contained eight peaks, at 245, 359, 382, 416, 446, 484, 537, and 635 nm. The absorption peak at 245 nm was considered as the charge transfer transition from the valence to the conduction band in the zirconia matrix [38–41]. However, the other 7 peaks were the results of the transitions from the  $^5\text{I}_8$  ground state to the  $^5\text{G}_2$ ,  $^5\text{G}_4 + ^3\text{K}_7$ ,  $^5\text{G}_5$ ,  $^3\text{K}_8 + ^5\text{F}_1 + ^5\text{G}_6$ ,  $^5\text{F}_3$ ,  $^5\text{F}_4 + ^5\text{S}_2$ , and  $^5\text{F}_5$  excited states of the  $\text{Ho}^{3+}$  ions [42,43]. An absorption band was found at 446 nm corresponding to the transition from  $^5\text{I}_8$  to  $^3\text{K}_8 + ^5\text{G}_6 + ^5\text{F}_1$  due to hypersensitivity, which obeyed the selection rules  $|\Delta s| = 0$ ,  $|\Delta l| \leq 2$ , and  $|\Delta j| \leq 2$ . This represented the sensitivity around  $\text{Ho}^{3+}$  in the matrix [44]. The absorption intensity was influenced by the concentrations of  $\text{Ho}^{3+}$ . Figure S2 (see Supplementary Materials) indicated that the absorption intensity was influenced by the concentrations of  $\text{Ho}^{3+}$ .

The optical band gap ( $E_g$ ) for the sample was calculated using the following formula [45]:

$$(\alpha h\nu)^2 = B(h\nu - E_g) \quad (4)$$

where  $\alpha$  was the absorption coefficient of the crystal sample,  $B$  was the constant, and  $h\nu$  was the energy of the absorbed photon. A plot of  $h\nu$  against  $(\alpha h\nu)^2$  was shown in Figure 9 and the point of intersection of the linear region with the X-axis gave an assessment of  $E_g$ . Values for the slopes, interceptions, regressions, and the optical band gaps  $E_g$  were presented in Table 4, which showed that the  $E_g$  of the  $(\text{ZrO}_2)_{90}(\text{Y}_2\text{O}_3)_{10-x}(\text{Ho}_2\text{O}_3)_x$  crystals were about 4.86 eV, and the crystals were wide bandgap materials. The optical band gaps of the  $\text{Ho}_2\text{O}_3$ :YSZ crystals were different from those in  $\text{Dy}_2\text{O}_3$ :YSZ crystals, where the optical band gap energy of the  $\text{Dy}_2\text{O}_3$ :YSZ crystals increased with  $\text{Dy}_2\text{O}_3$  contents [46].

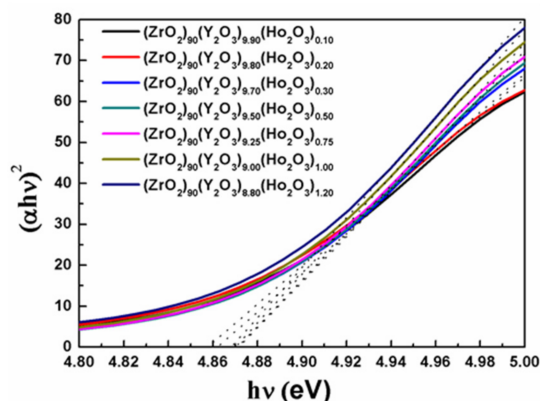


Figure 9. Measurements of the optical bandgap in  $(\text{ZrO}_2)_{90}(\text{Y}_2\text{O}_3)_{10-x}(\text{Ho}_2\text{O}_3)_x$  crystal discs.

Table 4. Values of intercept, slope,  $R^2$ , and  $E_g$  for  $(\text{ZrO}_2)_{90}(\text{Y}_2\text{O}_3)_{10-x}(\text{Ho}_2\text{O}_3)_x$ .

x	Slope	Intercept	$R^2$	$E_g$ (eV)
0.10	477	−2324	0.9998	4.86
0.30	557	−2714	0.9995	4.87
0.50	561	−2732	0.9995	4.87
0.75	577	−2812	0.9997	4.87
1.00	596	−2904	0.9998	4.87
1.20	611	−2974	0.9998	4.86

### 3.6.2. PL Spectra

The PL spectra of the  $(\text{ZrO}_2)_{90}(\text{Y}_2\text{O}_3)_{10-x}(\text{Ho}_2\text{O}_3)_x$  crystals under the excitation at 446 nm were shown in Figure 10.

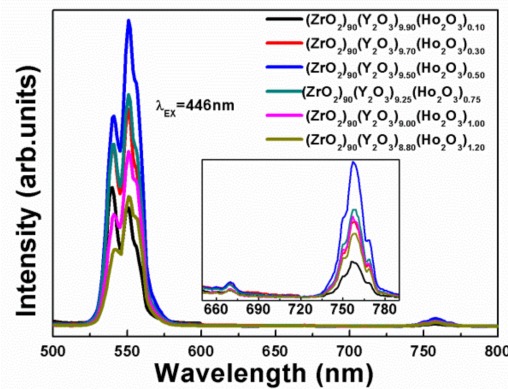


Figure 10. PL spectra of the  $(\text{ZrO}_2)_{90}(\text{Y}_2\text{O}_3)_{10-x}(\text{Ho}_2\text{O}_3)_x$  crystals under the excitation at 446nm.

The emission peaks at 540, 551, 670, and 757 nm correspond to the transitions from  $^5\text{S}_2$ ,  $^5\text{F}_4$ ,  $^5\text{F}_5$ , and  $^5\text{I}_4$  excited states to the  $^5\text{I}_8$  ground state  $\text{Ho}^{3+}$ , respectively [47]. Although their relative intensities varied, the emission peaks positions were independent of  $\text{Ho}_2\text{O}_3$  concentrations. For  $\text{Ho}_2\text{O}_3$  concentrations were between 0.30 and 1.20 mol%, the strongest green emission peak was at 551 nm ( $^5\text{S}_2 \rightarrow ^5\text{I}_8$ ), whereas the strongest green emission was at 540 nm ( $^5\text{F}_4 \rightarrow ^5\text{I}_8$ ) for the  $(\text{ZrO}_2)_{90}(\text{Y}_2\text{O}_3)_{9.90}(\text{Ho}_2\text{O}_3)_{0.10}$  sample.

At low  $\text{Ho}_2\text{O}_3$ -doped concentrations (0.10–0.50 mol%), the emission intensity increased with  $\text{Ho}_2\text{O}_3$  contents and reached the maximum at 0.50 mol%, then decreased with higher  $\text{Ho}_2\text{O}_3$  contents (0.50–1.20 mol%) due to the concentration quenching effect.

The energy diagram of  $\text{Ho}^{3+}$  in  $\text{Ho}_2\text{O}_3$  doped YSZ crystals with the radiative and non-radiative transitions were shown in Figure 11. The probability of non-radiative relaxation from  $^5\text{F}_4$  to  $^5\text{S}_2$  increased with  $\text{Ho}^{3+}$  concentration. Therefore, for samples with  $\text{Ho}_2\text{O}_3$  concentrations higher than 0.30 mol%, the emission peak at 551 nm ( $^5\text{S}_2 \rightarrow ^5\text{I}_8$ ) was higher than that at 540 nm ( $^5\text{F}_4 \rightarrow ^5\text{I}_8$ ).

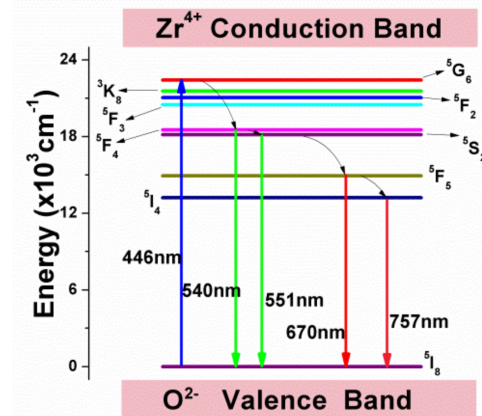


Figure 11. The energy diagram of  $\text{Ho}^{3+}$  in  $\text{Ho}_2\text{O}_3$  doped YSZ crystals with the radiative and non-radiative transitions.

Based on the Dexter theory [48], the concentration quenching effect via an electric multipole moment interaction was given by the formula [49]:

$$\frac{I}{y} = k \left( 1 + \beta y^\theta \right)^{-1} \quad (5)$$

$$\log\left(\frac{I}{y}\right) = -\frac{\theta}{3} \log(y) + k \quad (6)$$

where  $I$  was the luminous intensity,  $k$  was a constant,  $x$  and  $y$  were the concentrations of  $\text{Ho}_2\text{O}_3$  and  $\text{Ho}^{3+}$ , respectively. It was obvious that  $y = 2x$ . The values for  $\theta$  of 3, 6,

8, and 10 represented exchange, electric dipole–dipole interaction, dipole–quadrupole, and quadrupole–quadrupole interactions, respectively [49]. The slope of the fitted line in Figure 12 was  $-1.95$ , or  $\theta \approx 6$ , this suggested that the quenching effect occurred via an electric dipole–dipole interaction between closest neighbor  $\text{Ho}^{3+}$  ions.

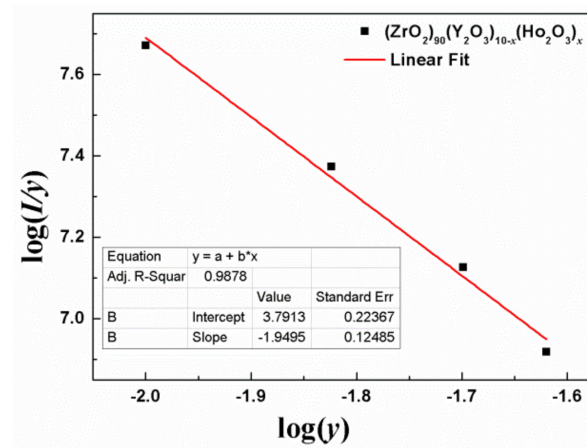


Figure 12. Relationship between  $\log(I/y)$  vs.  $\log(y)$  in  $(\text{ZrO}_2)_{90}(\text{Y}_2\text{O}_3)_{10-x}(\text{Ho}_2\text{O}_3)_x$  crystals.

### 3.6.3. Color Coordinate

The measurement of color coordinates of a light source was an important method for characterizing its quality. In general, the overall emitted color was represented by the CIE chromaticity coordinate  $(x, y)$  [50,51].

The color coordinates of the  $(\text{ZrO}_2)_{90}(\text{Y}_2\text{O}_3)_{10-x}(\text{Ho}_2\text{O}_3)_x$  crystals were shown in Figure 13 and the color purity of  $(\text{ZrO}_2)_{90}(\text{Y}_2\text{O}_3)_{9.50}(\text{Ho}_2\text{O}_3)_{0.50}$  crystal calculated by CIE1931. The overall color coordinates of the emission spectra from the crystal samples were all in the green region near 551 nm and the color coordinates of the  $(\text{ZrO}_2)_{90}(\text{Y}_2\text{O}_3)_{9.50}(\text{Ho}_2\text{O}_3)_{0.50}$  crystal were  $(0.307, 0.683)$ .

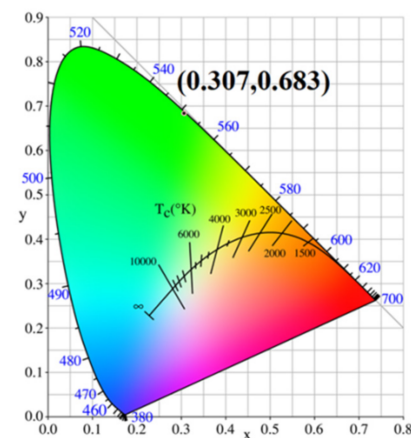


Figure 13. Color coordinates of  $(\text{ZrO}_2)_{90}(\text{Y}_2\text{O}_3)_{9.50}(\text{Ho}_2\text{O}_3)_{0.50}$  crystal.

Color purity could be calculated by the formula:

$$\text{Color purity} = \frac{\sqrt{(x - x_i)^2 + (y - y_i)^2}}{\sqrt{(x_d - x_i)^2 + (y_d - y_i)^2}} \times 100\% \quad (7)$$

where  $(x, y)$ ,  $(x_i, y_i)$ , and  $(x_d, y_d)$  represented the color coordinates of the emission spectrum of the sample, the coordinates of the light source and the main wavelength of the light source,

respectively. The value calculated for the color purity of the  $(\text{ZrO}_2)_{90}(\text{Y}_2\text{O}_3)_{9.50}(\text{Ho}_2\text{O}_3)_{0.50}$  crystal sample was 99.6% and thus was suitable for use in green light-emitting devices.

In addition, the relative color temperature (CCT) could be calculated by McCamy's formula [52]:

$$\text{CCT} = -449n^3 + 3525n^2 - 6823n + 5520.33 \quad (8)$$

where  $n = (x - x_e)/(y - y_e)$  was the inverse slope of the line. The color coordinates  $x_e = 0.332$ ,  $y_e = 0.186$ , which was obtained by extending the isochromatic temperature lines on the CIE1931xy chromaticity diagram down to a point. The CCT values, as shown in Table 5, were near 5700 K for each of the crystals. This was close to the color temperature value of household appliance lighting.

**Table 5.** Chromaticity coordinates ( $x$ ,  $y$ ) for  $(\text{ZrO}_2)_{90}(\text{Y}_2\text{O}_3)_{10-x}(\text{Ho}_2\text{O}_3)_x$  crystals.

$x$	CIE $x$	CIE $y$	CCT
0.10	0.2977	0.6891	5777
0.30	0.3020	0.6877	5745
0.50	0.3072	0.6835	5707
1.00	0.3093	0.6822	5693
1.20	0.3129	0.6786	5667

#### 4. Conclusions

A series of  $(\text{ZrO}_2)_{90}(\text{Y}_2\text{O}_3)_{10-x}(\text{Ho}_2\text{O}_3)_x$  ( $x = 0.00, 0.10, 0.20, 0.30, 0.50, 0.75, 1.00, 1.20$ ),  $(\text{ZrO}_2)_{92}(\text{Y}_2\text{O}_3)_8$  and  $(\text{ZrO}_2)_{92}(\text{Y}_2\text{O}_3)_{7.25}(\text{Ho}_2\text{O}_3)_{0.75}$  single crystals were successfully grown and stabled in tetragonal phase. The results of positron annihilation lifetime spectra indicated that the increase in  $\text{Y}_2\text{O}_3$  concentration led to the increases of defects and mean positron lifetime, which enhanced the scattering of light and reduced the luminous intensity and the quantum yields of the crystals. Optical absorption spectra of  $(\text{ZrO}_2)_{90}(\text{Y}_2\text{O}_3)_{10-x}(\text{Ho}_2\text{O}_3)_x$  crystals showed peaks at 359, 382, 416, 446, 484, 537, and 635 nm corresponding to the transitions from the  $^5\text{I}_8$  ground state to  $^5\text{G}_3$ ,  $^5\text{G}_4 + ^3\text{K}_7$ ,  $^5\text{G}_5$ ,  $^3\text{K}_8 + ^5\text{F}_1 + ^5\text{G}_6$ ,  $^5\text{F}_3$ ,  $^5\text{F}_4 + ^5\text{S}_2$ , and  $^5\text{F}_5$  excited states of  $\text{Ho}^{3+}$ , respectively. The samples all had an optical bandgap of about 4.86 eV. Under excitation with 446 nm, strong green light and weak near-red emissions were observed at 540, 551, 670, and 757 nm. The concentration quenching occurred when the concentration of  $\text{Ho}_2\text{O}_3$  was above 0.50 mol%. This suggested that the quenching effect occurred via an electric dipole–dipole interaction between closest neighbor  $\text{Ho}^{3+}$  ions. The color purity calculated by CIE1931 was >99%. All results show the samples have good prospects for applications in green light-emitting devices.

**Supplementary Materials:** The following supporting information can be downloaded at: <https://www.mdpi.com/article/10.3390/cryst12030415/s1>, Figure S1. Positron annihilation lifetime spectra of  $(\text{ZrO}_2)_{92}(\text{Y}_2\text{O}_3)_{7.25}(\text{Ho}_2\text{O}_3)_{0.75}$  and  $(\text{ZrO}_2)_{90}(\text{Y}_2\text{O}_3)_{9.25}(\text{Ho}_2\text{O}_3)_{0.75}$  crystals; Figure S2. UV-vis absorption spectra of the  $(\text{ZrO}_2)_{90}(\text{Y}_2\text{O}_3)_{10-x}(\text{Ho}_2\text{O}_3)_x$  crystal discs.

**Author Contributions:** Conceptualization, Y.Y. and S.X.; methodology, Y.Y.; software, Y.Y. and Y.P.; validation, Y.Y., S.X. and W.D.; formal analysis, Y.Y., S.L. and Z.C.; investigation, S.X.; resources, W.D.; data curation, Y.Y., W.W. and X.H.; writing—original draft preparation, Y.Y.; writing—review and editing, Y.Y. and W.D.; visualization, D.W.; supervision, W.D.; project administration, Y.Y. and W.D. All authors have read and agreed to the published version of the manuscript.

**Funding:** This work was financially supported by the Natural Science Foundations of China under Grant Nos. 11975004 and 12175047, the Key Research and Development Plan Project of Guangxi, China under Grant No. Guike AB18281007 and Education Department of Guangxi Zhuang Autonomous Region (No. 2021KY0017).

**Data Availability Statement:** The data presented in this study are available on reasonable request from the corresponding author.

**Acknowledgments:** The authors gratefully thank Bernard A. Goodman, Dingkang Xiong and Yuyang Huang for useful discussions on the subject matter of this paper.

**Conflicts of Interest:** The authors declare no conflict of interest.

## References

1. Zhang, X.; Cao, C.; Zhang, C.; Xie, S.; Xu, G.; Zhang, J.; Wang, X. Photoluminescence and energy storage traps in CaTiO<sub>3</sub>:Pr<sup>3+</sup>. *Mater. Res. Bull.* **2010**, *45*, 1832–1836. [[CrossRef](#)]
2. Yuan, J.; Wang, W.; Ye, Y.; Deng, T.; Huang, Y.; Gu, S.; Chen, Y.; Xiao, P. 2.0 μm Ultra Broadband Emission from Tm<sup>3+</sup>/Ho<sup>3+</sup> Co-Doped Gallium Tellurite Glasses for Broadband Light Sources and Tunable Fiber Lasers. *Crystals* **2021**, *11*, 190. [[CrossRef](#)]
3. Buarque, J.M.M.; Manzani, D.; Scarpari, S.L.; Nalin, M.; Ribeiro, S.J.L.; Esbenschade, J.; Schiavon, M.A.; Ferrariet, J.L. SiO<sub>2</sub>-TiO<sub>2</sub> doped with Er<sup>3+</sup>/Yb<sup>3+</sup>/Eu<sup>3+</sup> photoluminescent material: A spectroscopy and structural study about potential application for improvement of the efficiency on solar cells. *Mater. Res. Bull.* **2018**, *107*, 295–307. [[CrossRef](#)]
4. Liu, L.; Sun, Z.; Ma, C.; Tao, R.; Zhang, J.; Li, H.; Zhao, E. Highly sensitive and accurate optical thermometer through Er doped tellurite glasses. *Mater. Res. Bull.* **2018**, *105*, 306–311. [[CrossRef](#)]
5. Sreedhar, V.B.; Basavapoornima, C.; Jayasankar, C.K. Spectroscopic and fluorescence properties of Sm<sup>3+</sup>-doped zincfluorophosphate glasses. *J. Rare Earths* **2014**, *32*, 918–926. [[CrossRef](#)]
6. Neelima, G.; Kummara, V.K.; Ravi, N.; Suresh, K.; Rasool, S.N.; Tyagarajan, K.; Prasad, T.J. Investigation of spectroscopic properties of Sm<sup>3+</sup>-doped oxyfluorophosphate glasses for laser and display applications. *Mater. Res. Bull.* **2018**, *110*, 223–229. [[CrossRef](#)]
7. Singh, V.; Annapurna Devi, C.B.; Kaur, S.; Rao, A.S.; Singh, N. Optical properties of Sr<sub>2</sub>La<sub>8</sub>(SiO<sub>4</sub>)<sub>6</sub>O<sub>2</sub> doped with Ho<sup>3+</sup> phosphor. *Optik* **2021**, *242*, 167268. [[CrossRef](#)]
8. Sarkar, J.; Mondal, S.; Panja, S.; Dey, I.; Sarkar, A.; Ghorai, U.K. Multicolour tuning and perfect white emission from novel PbWO<sub>4</sub>:Yb<sup>3+</sup>:Ho<sup>3+</sup>:Tm<sup>3+</sup> nanophosphor. *Mater. Res. Bull.* **2019**, *112*, 314–322. [[CrossRef](#)]
9. Xu, Y.; Wang, Y.; Shi, L.; Xing, L.; Tan, X. Bright white upconversion luminescence in Ho<sup>3+</sup>/Yb<sup>3+</sup>/Tm<sup>3+</sup> triple doped CaWO<sub>4</sub> polycrystals. *Opt. Laser Technol.* **2013**, *54*, 50–52. [[CrossRef](#)]
10. Zhang, Y.; Huang, F.; Liu, L.; Liu, X.; Zheng, S.; Chen, D. Pr<sup>3+</sup>/Ho<sup>3+</sup> co-doped glass phosphors for application in warm white light-emitting diodes. *Mater. Lett.* **2016**, *167*, 1–3. [[CrossRef](#)]
11. Ming, C.; Song, F.; Yu, Y.; Wang, Q. Impact of Ce<sup>4+</sup> ion on microstructure and luminescence character of Ho<sup>3+</sup>/Yb<sup>3+</sup> co-doped ZrO<sub>2</sub> nanocrystal. *J. Alloys Compd.* **2012**, *512*, 121–123. [[CrossRef](#)]
12. John Berlin, I.; Lakshmi, J.S.; Sujatha Lekshmy, S.; Daniel, G.P.; Thomas, P.V.; Joy, K. Effect of sol temperature on the structure, morphology, optical and photoluminescence properties of nanocrystalline zirconia thin films. *J. Sol-Gel Sci. Technol.* **2011**, *58*, 669–676. [[CrossRef](#)]
13. Liang, F.; Chen, J.; Cheng, J.; Jiang, S.P.; He, T.; Pu, J.; Li, J. Novel nano-structured Pd<sup>+</sup> yttrium doped ZrO<sub>2</sub> cathodes for intermediate temperature solid oxide fuel cells. *Electrochem. Commun.* **2008**, *10*, 42–46. [[CrossRef](#)]
14. Di Monte, R.; Kašpar, J. Heterogeneous environmental catalysis—A gentle art: CeO<sub>2</sub>-ZrO<sub>2</sub> mixed oxides as a case history. *Catal. Today* **2005**, *100*, 27–35. [[CrossRef](#)]
15. Hafele, E.; Kaltenmaier, K.; Schtinauer, U. Application of the ZrO<sub>2</sub> Sensor in Determination of Pollutant Gases. *Sens. Actuators B* **1991**, *4*, 525–527. [[CrossRef](#)]
16. Sathyaseelan, B.; Manikandan, E.; Baskaran, I.; Senthilnathan, K.; Sivakumar, K.; Moodley, M.K.; Ladchumanandasivam, R.; Maaza, M. Studies on structural and optical properties of ZrO<sub>2</sub> nanopowder for opto-electronic applications. *J. Alloys Compd.* **2017**, *694*, 556–559. [[CrossRef](#)]
17. French, R.H.; Glass, S.J.; Ohuchi, F.S.; Xu, Y.; Ching, W.Y. Experimental and theoretical determination of the electronic structure and optical properties of three phases of ZrO<sub>2</sub>. *Phys. Rev. B Condens. Matter.* **1994**, *49*, 5133–5142. [[CrossRef](#)]
18. Viazzi, C.; Bonino, J.P.; Ansart, F.; Barnabé, A. Structural study of metastable tetragonal YSZ powders produced via a sol-gel route. *J. Alloys Compd.* **2008**, *452*, 377–383. [[CrossRef](#)]
19. Morinaga, M.; Adachi, H.; Tsukada, M. Electronic structure and phase stability of ZrO<sub>2</sub>. *J. Phys. Chem. Solids* **1983**, *44*, 301–306. [[CrossRef](#)]
20. Barabás, R.; Fort, C.I.; Turdean, G.L.; Bizo, L. Influence of HAP on the Morpho-Structural Properties and Corrosion Resistance of ZrO<sub>2</sub>-Based Composites for Biomedical Applications. *Crystals* **2021**, *11*, 202. [[CrossRef](#)]
21. Schubert, H. Anisotropic Thermal Expansion Coefficients of Y<sub>2</sub>O<sub>3</sub>-Stabilized Tetragonal Zirconia. *J. Am. Ceram. Soc.* **1986**, *69*, 270–271. [[CrossRef](#)]
22. Wang, D.N.; Xu, S.L.; Wang, X.Y.; Li, S.Y.; Hong, X.; Goodman, B.A.; Deng, W. Crystal growth, structure and optical properties of Pr<sup>3+</sup>-doped yttria-stabilized zirconia single crystals. *Chin. Phys. B* **2021**, *30*, 078103. [[CrossRef](#)]
23. Srigurunathan, K.; Meenambal, R.; Guleria, A.; Kumar, D.; Ferreira, J.; Kannan, S. Unveiling the Effects of Rare-Earth Substitutions on the Structure, Mechanical, Optical, and Imaging Features of ZrO<sub>2</sub> for Biomedical Applications. *ACS Biomater. Sci. Eng.* **2019**, *5*, 1725–1743. [[CrossRef](#)] [[PubMed](#)]

24. Popov, V.V.; Menushenkov, A.P.; Yastrebtev, A.A.; Tsarenko, N.A.; Arzhatkina, L.A.; Shchetinin, I.V.; Zheleznyi, M.V.; Ponkratov, K.V. Regularities of formation of complex oxides with the fluorite structure in the  $ZrO_2$ - $Y_2O_3$  system. *Russ. J. Inorg. Chem.* **2017**, *62*, 1147–1154. [[CrossRef](#)]
25. Cruz, R.M.; Pareja, R.; Gonzalez, R. Effect of thermochemical reduction on the electrical, optical-absorption, and positron-annihilation characteristics of ZnO crystals. *Phys. Rev. B* **1992**, *45*, 6581–6586. [[CrossRef](#)]
26. Dutta, S.; Chattopadhyay, S.; Jana, D.; Banerjee, A.; Manik, S.; Pradhan, S.K.; Sutradhar, M.; Sarkar, A. Annealing effect on nano-ZnO powder studied from positron lifetime and optical absorption spectroscopy. *J. Appl. Phys.* **2006**, *100*, 114328. [[CrossRef](#)]
27. Brandt, W.; Paulin, R. Positron Diffusion in Solids. *Phys. Rev. B* **1972**, *5*, 2430–2435. [[CrossRef](#)]
28. Nambissan, P.M.G. Nano sulfide and oxide semiconductors as promising materials for studies by positron annihilation. *J. Phys. Conf. Ser.* **2013**, *443*, 012040. [[CrossRef](#)]
29. Šćepanović, M.; de Castro, V.; García-Cortés, I.; Sánchez, F.J.; Gigl, T.; Hugenschmidt, C.; Leguey, T. Characterisation of open volume defects in Fe–Cr and ODS Fe–Cr alloys after He<sup>+</sup> and Fe<sup>+</sup> ion irradiations. *J. Nucl. Mater.* **2020**, *538*, 152230. [[CrossRef](#)]
30. Anwand, W.; Skorupa, W.; Schumann, T.; Posselt, M.; Schmidt, B.; Grötzschel, R.; Brauer, G. Implantation-caused open volume defects in Ge after flash lamp annealing (FLA) probed by slow positron implantation spectroscopy (SPIS). *Appl. Surf. Sci.* **2008**, *255*, 81–83. [[CrossRef](#)]
31. Kesavulu, C.R.; Kim, H.J.; Lee, S.W.; Kaewkhao, J.; Wantana, N.; Kothan, S.; Kaewjaeng, S. Optical spectroscopy and emission properties of Ho<sup>3+</sup>-doped gadolinium calcium silicoborate glasses for visible luminescent device applications. *J. Non-Cryst. Solids* **2017**, *474*, 50–57. [[CrossRef](#)]
32. Zhao, Y.; Zhai, X.; Yan, D.; Zhao, Y.; Zhou, H.; Zhao, X.; Li, J.; Jin, H. The effect of artificial stress on Er<sup>3+</sup> doped perovskite lead-free piezoceramics. *J. Alloys Compd.* **2017**, *709*, 724–728. [[CrossRef](#)]
33. Zhao, Y.; Ge, Y.; Zhang, X.; Zhao, Y.; Zhou, H.; Li, J.; Jin, H. Comprehensive investigation of Er<sub>2</sub>O<sub>3</sub> doped (Li,K,Na)NbO<sub>3</sub> ceramics rendering potential application in novel multifunctional devices. *J. Alloys Compd.* **2016**, *683*, 171–177. [[CrossRef](#)]
34. Lin, J.; Lu, Q.; Xu, J.; Wu, X.; Lin, C.; Lin, T.; Chen, C.; Luo, L.H. Outstanding optical temperature sensitivity and dual-mode temperature-dependent photoluminescence in Ho<sup>3+</sup>-doped (K,Na)NbO<sub>3</sub>-SrTiO<sub>3</sub> transparent ceramics. *J. Am. Ceram. Soc.* **2019**, *102*, 4710–4720. [[CrossRef](#)]
35. Ishida, H.; Bünzli, J.C.; Beeby, A. Guidelines for measurement of luminescence spectra and quantum yields of inorganic and organometallic compounds in solution and solid state (IUPAC Technical Report). *Pure Appl. Chem.* **2016**, *88*, 701–711. [[CrossRef](#)]
36. Ishida, H.; Tobita, S.; Hasegawa, Y.; Katoh, R.; Nozaki, K. Recent advances in instrumentation for absolute emission quantum yield measurements. *Coord. Chem. Rev.* **2010**, *254*, 2449–2458. [[CrossRef](#)]
37. Katoh, R.; Suzuki, K.; Furube, A.; Kotani, M.; Tokumaru, K. Fluorescence Quantum Yield of Aromatic Hydrocarbon Crystals. *J. Phys. Chem. C* **2009**, *113*, 2961–2965. [[CrossRef](#)]
38. Upadhyaya, D.D.; Ghosh, A.; Gurumurthy, K.R.; Ram, P. Microwave sintering of cubic zirconia. *Ceram. Int.* **2001**, *27*, 415–418. [[CrossRef](#)]
39. Soares, M.R.N.; Soares, M.J.; Fernandes, A.J.S.; Rino, L.; Costa, F.M.; Monteiro, T. YSZ:Dy<sup>3+</sup> single crystal white emitter. *J. Mater. Chem.* **2011**, *21*, 15262–15265. [[CrossRef](#)]
40. Manjunatha, S.; Dharmaprakash, M.S. Microwave assisted synthesis of cubic Zirconia nanoparticles and study of optical and photoluminescence properties. *J. Lumin.* **2016**, *180*, 20–24. [[CrossRef](#)]
41. Rosa, E.D.L.; Diaz-Torres, L.A.; Salas, P.; Rodríguez, R.A. Visible light emission under UV and IR excitation of rare earth doped ZrO<sub>2</sub> nanophosphor. *Opt. Mater.* **2005**, *27*, 1320–1325. [[CrossRef](#)]
42. Wang, C.; Chen, X.B.; Zhang, C.L.; Zhang, Y.Z.; Liu, J.Y.; Wang, Y.F.; Liu, D.H.; Du, S.; Xu, X.L.; Wang, L.; et al. Optical parameters and energy levels splitting of Ho<sup>3+</sup> in Ho<sup>3+</sup> GdVO<sub>4</sub>. *Chin. Phys. B* **2008**, *17*, 4656–4664.
43. Wang, H.; Yang, Q.; Sun, Y.; Jiang, X.; Huang, D. Optical spectroscopy studies of Ho/Yb co-doped yttrium lanthanum oxide transparent ceramics. *J. Lumin.* **2017**, *192*, 752–756. [[CrossRef](#)]
44. Jayachandra Prasad, T.; Neelima, G.; Ravi, N.; Kiran, N.; Nallabala, N.K.; Kummara, V.K.; Suresh, K.; Gadige, P. Optical and spectroscopic properties of Ho<sup>3+</sup>-doped fluorophosphate glasses for visible lighting applications. *Mater. Res. Bull.* **2020**, *124*, 110753.
45. Priyanka, R.; Arunkumar, S.; Basavapoornima, C.; Mary Mathelane, R.; Marimuthu, K. Structural and spectroscopic investigations on Eu<sup>3+</sup> ions doped boro-phosphate glasses for optical display applications. *J. Lumin.* **2020**, *220*, 116964. [[CrossRef](#)]
46. Hong, X.; Xu, S.; Wang, X.; Wang, D.; Li, S.; Goodman, B.A.; Deng, W. Growth, structure and optical spectroscopic properties of dysprosia-doped cubic yttria stabilized zirconia (YSZ) single crystals. *J. Lumin.* **2021**, *231*, 117766. [[CrossRef](#)]
47. Lim, C.S.; Aleksandrovsky, A.; Molokeev, M.; Oreshonkov, A.; Atuchin, V. Structural and Spectroscopic Effects of Li<sup>+</sup> Substitution for Na<sup>+</sup> in Li<sub>x</sub>Na<sub>1-x</sub>CaGd<sub>0.5</sub>Ho<sub>0.05</sub>Yb<sub>0.45</sub>(MoO<sub>4</sub>)<sub>3</sub> Scheelite-Type Upconversion Phosphors. *Molecules* **2021**, *26*, 7357. [[CrossRef](#)]
48. Dexter, D.L. A theory of sensitized luminescence in solids. *J. Chem. Phys.* **1953**, *21*, 836–850. [[CrossRef](#)]
49. Kalimuthu, K.R.; Moorthy Babu, S.; Kalimuthu, V. Synthesis and photoluminescence properties of Sm<sup>3+</sup> doped LiGd(WO<sub>4</sub>)<sub>2</sub> phosphors with high color purity. *Opt. Mater.* **2020**, *102*, 109804.
50. Gavenda, T.; Gedeon, O.; Jurek, K. Volume changes in glass induced by an electron beam. *Nucl Instrum Methods. Phys. Res. B* **2014**, *322*, 7–12.

- 
51. Das, S.; Lalla, N.P.; Okram, G.S. Synthesis, characterization and dielectric properties of nanocrystalline nickel. *Indian J. Pure Appl. Phys.* **2014**, *52*, 386–390.
  52. McCamy, C.S. Correlated Color Temperature as an Explicit Function of Chromaticity Coordinates. *Color Res. Appl.* **1992**, *17*, 142–144. [[CrossRef](#)]